Oxide ion and proton conductivity in a family of highly oxygen deficient perovskite derivatives

Chloe A. Fuller†, Douglas A. Blom‡, Thomas Vogt††, Ivana Radosavljevic Evans†,*, and John S. O. Evans†,*

† Department of Chemistry, Durham University, Science Site, South Road, Durham DH1 3LE, United Kingdom

‡ Department of Chemical Engineering and NanoCenter, University of South Carolina, Columbia, SC 29208, USA

†† Department of Chemical Engineering, Chemistry and Biochemistry and NanoCenter, University of South Carolina, Columbia, SC 29208, USA

ABSTRACT: Functional oxides showing high ionic conductivity have many important technological applications. We report oxide ion and proton conductivity in a family of perovskite-related compounds of general formula $A_3OhTd_2O_{7.5}$ where Oh is an octahedrally and Td a tetrahedrally coordinated metal ion. The high tetrahedral content in these $ABO_{2.5}$ compositions relative to that in perovskite ABO_3 or brownmillerite $A_2B_2O_5$ structures leads to tetrahedra with only three of their four vertices connected in the polyhedral framework, imparting a potential low-energy mechanism for O^{2-} migration. The low and high temperature average and local structures of $Ba_3YGa_2O_7$ ($P2/c$ a = 7.94820(5) Å, b = 5.96986(4) Å, c = 18.4641(1) Å and β = 91.2927(5) ° at 22 °C) are determined by Rietveld and neutron pair distribution function (PDF) analysis, and a phase transition to a high temperature $P112_1/a$ (a = 12.0602(1) Å, b = 9.8282(2) Å, c = 8.04982(6) Å and γ = 107.844(3)° at 1000 °C) structure involving migration of O^{2-} ions is identified. Ionic conductivities of $Ba_3YGa_2O_{7.5}$ and compositions substituted to introduce additional oxide vacancies and interstitials are reported. Most phases show proton conductivity at lower temperatures and oxide ion conductivity at high temperature, with $Ba_3YGa_2O_{7.5}$ retaining proton conductivity to high temperature. $Ba_{2.9}La_{0.1}YGa_2O_{7.55}$ and $Ba_3YGa_{1.9}Ti_{0.1}O_{7.55}$ appear to be dominant oxide-ion conductors with conductivities an order of magnitude higher than the parent compound.

INTRODUCTION

Solid ionic conductors are an important class of crystalline materials characterized by their ability to transport current via the diffusion of ions (here O^{2-} and H^+) through the structure. This valuable property can be harnessed for a wide range of technological applications, including oxygen sensors and pumps,[1] separation membranes[2] and electrolyte materials in solid oxide fuel cells.[3] Understanding how specific elemental compositions, structural features and microscopic dynamics underpin high conductivity is vital for the development of new materials. In particular, it may pave the way to devices that can operate at lower temperatures than current technology, giving significant cost and durability benefits. In this paper we report high conductivity in a new family of perovskite derivatives using the design concept of incorporating "flexible tetrahedra" into the solid state structure.

After the well-known fluorite derivatives (stabilized zirconias, δ-Bi_2O_3, etc.), some of the best performing oxide ion conductors are perovskite derivatives of composition $ABO_{3-\delta}$. These can be broadly split into two categories: $A^{III}B^{III}O_3$-derived compounds where conductivity is typically maximized for $\delta \lesssim 0.2$; and $A^{II}B^{IV}O_3$ to $A^{II}B^{III}O_{2.5}$ compositions which either retain the disordered perovskite structure or order to structure types such as brownmillerite as δ increases. This latter family tends to have maximum conductivities for higher values of δ. For example, $Ba_2In_2O_5$ has the brownmillerite structure and contains alternate layers of fully corner-linked octahedra and tetrahedra—$OhO_{6/2}$ and $TdO_{4/2}$, respectively, in Niggli formalism.[4] In its low-temperature ordered structure it shows moderate O^{2-} conductivity ($\sigma \approx 10^{-4}$ S cm^{-1} at 750 °C), but the conductivity rises ($\sigma \approx 10^{-1}$ S cm^{-1} at 950 °C) above phase transitions to a tetragonal then cubic structure where the tetrahedral ordering is lost.[5] Its conductivity is one of the highest in the $BaZr_{1-x}In_xO_{3-x/2}$ series.[6]

Tetrahedral disorder is a common feature in several other O^{2-} conductors including Ge-apatites,[7-12] scheelites,[13-18] melilites,[19-20] derivatives of the δ-Bi_2O_3 structure,[21-23] $La_2Mo_2O_9$[24-25] and other brownmillerites.[26-27] The structural flexibility imparted by the tetrahedral units promotes the stabilization and transport of oxygen interstitial or vacancy defects, enhancing ionic conductivity. There is also significant literature precedence that tetrahedra that are not fully linked to other framework polyhedra (e.g. $TdO_{3/2}O$ groups) can give oxide ion mobility at low temperatures. Terminal oxygens are reported to facilitate rotations of the Td_2O_8 groups in ZrW_2O_8[28] and related compounds $Zr_{1-x}Sn_xMo_2O_8$[29] below room temperature, and they were identified as a critical structural feature underpinning the high conductivity of various melilites.[19]

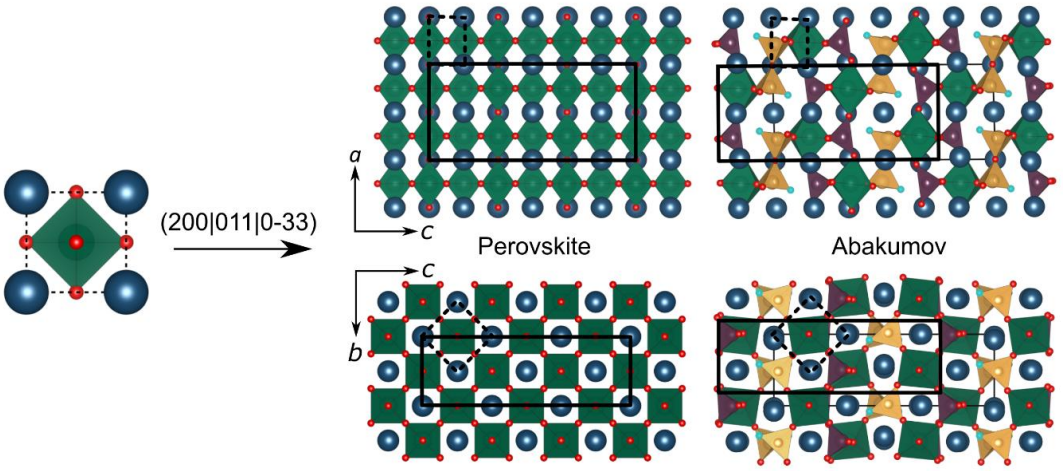

Figure 1. Relationship between the perovskite structure (left) and the $A_3OhTd_2O_{7.5}$ structure proposed by Abakumov *et al.* (right). The unit cells of both structures are shown in dotted and bold solid lines respectively, viewed from two different directions; origin shifts are shown in the right hand figures. The numbers above the arrow indicate the transformation matrix needed to go from the perovskite to the $A_3OhTd_2O_{7.5}$ structure. Blue, green and red colors indicate the A, B/Oh and O sites respectively; purple and yellow show the Td sites, with yellow used to highlight the Td_2O_7 tetrahedra containing terminal O

We have recently reported high O^{2-} conductivity in $Sr_2Sc_{0.6}Zn_{0.4}GaO_{4.8}$[27] which has the average structure of a highly oxygen deficient $ABO_{2.4}$ perovskite, but was designed using similar ideas to those of Chernov *et al.*[30] to contain a ~2:1 ratio of cations favoring tetrahedral coordination over octahedral, such that its formula can better expressed as $Sr_3(Sc_{0.9}Zn_{0.1})_{Oh}(Zn_{0.9}Ga_{1.1})_{Td}O_{7.2}$. Total scattering (PDF) studies revealed that its local structure was closely related to that of a family of $A_3OhTd_2O_{7.5}$ compounds, that are shown on the right of Figure 1. Crucially, this structure contains a TdO_4 tetrahedron with only three of its four corners linked to the other framework polyhedra ($TdO_{3/2}O$), and we suggested that the one-coordinate oxygen atoms and the associated structural flexibility were linked to the substantial increase in conductivity seen in $Sr_2Sc_{0.6}Zn_{0.4}GaO_{4.8}$ relative to its Sr_2ScGaO_5 brownmillerite parent.

Several compounds with this $A_3(OhO_{6/2})(TdO_{4/2})(TdO_{3/2}O)$ connectivity are known but have not, to our knowledge, been studied in the context of ionic conductivity. The earliest work we are aware of is by Kovba *et al.* who reported $A_3OhTd_2O_{7.5}$ compounds following explorations of the $BaO–Y_2O_3–Al_2O_3$[31] and $BaO-Ln_2O_3-Ga_2O_3$[32] (Ln = lanthanide) phase diagrams. Their work was later expanded on by Abakumov *et al.* who discussed the structure of compounds with A = Ba, Oh = Ln/Y and Td = Ga/Al.[33] The room temperature structures were described with perovskite-related unit cells (V = 12×$V_{perovskite}$) as shown in Figure 1. They contain infinite 2D slabs of $^2_\infty[(0hO_{6/2})(TdO_{4/2})]^{4-}$ fully-connected polyhedra perpendicular to the longest cell axis. These are interleaved by layers containing Td_2O_7 groups which have two of their four corners unconnected to the rest of the framework ($OO_{2/2}Td\text{-}O\text{-}TdO_{2/2}O$). A-site cations sit in four different perovskite-like sites within this framework with coordination numbers of 10, 8, 11 and 10 (average 10 when site multiplicities taken into account). It is worth noting that the addition of extra O atoms on the sites between Td_2O_7 groups along *a* and midway between each purple and yellow tetrahedron of Figure 1 would create the ABO_3 fully-connected perovskite framework.

Monoclinic space groups $P2/c$ or Pc were reported for Ga and Al compounds, respectively, with monoclinic angles of ~91.2°. Coordinates were only reported for $P2/c$ $Ba_3ErGa_2O_{7.5}$ (hereafter referred to as the Abakumov structure). A few other compounds have since been shown to adopt similar monoclinic structures, including $Ba_3YCo_2O_{7.5}$,[34] $Ba_3YFe_2O_{7.5}$,[35] $Na_3MnV_2O_{7.5}$[36] and $(K_{1/3}Ca_{2/3})_3CaSi_2O_{7.5}$[37] with all four being assigned the space group $P2/c$ at room temperature. The latter two compounds have a metrically orthorhombic cell, with reported monoclinic angles very close to 90° (90.03° and 90.005°, respectively). Compounds in the $Sr_3LnAl_2O_{7.5}$ series (Ln = Tb to Lu) have the same polyhedral connectivity, but have a different polyhedral tilting pattern, resulting in space group $C2$.[38]

Interestingly, related structures with different tetrahedral ordering patterns within the Td_2O_7 layers have also been identified in some silicate systems by Tamazyan *et al.* ($Na_2Ba_6Si_4O_{15}$)[39] and Kahlenberg *et al.* ($Na_2Ca_6Si_4O_{15}$).[40] This ordering is compared to the Abakumov pattern in Figure 2a and Figure 2b. In the Abakumov structure, Td_2O_7 groups have the same positions between each ($OhO_{6/2}$)($TdO_{4/2}$) fully-connected slab. In the Tamazyan ordering they are offset by $a/2$ of the Abakumov cell. The Tamazyan-type ordering means that the unit cell becomes monoclinic with cell parameters a≈11, b≈9, c≈7 Å and γ≈107° in space group $P112_1/a$. These two orderings correspond to alternate choices for removing oxygens in the hypothetical transformation from the perovskite to Abakumov connec-

tivity. As shown in Figure 2c, a disordered material containing a mixture of these two Td_2O_7 positions would, on average, display orthorhombic symmetry with highest space-group symmetry *Cmcm*.

In fact, several of these compounds have been reported to undergo phase transitions to orthorhombic symmetry at high temperature. Abakumov reported that a monoclinic-to-orthorhombic transition happens between 177 and 377 °C for different compounds, with the transition temperature increasing with the size of the Ln atom. While full structural models of the high temperature phase were not reported, high temperature electron diffraction data were used to confirm orthorhombic symmetry for $Ba_3LnAl_2O_{7.5}$, with space group *Cmc*2$_1$ suggested. If the phase transition involves oxygen disorder along the Td_2O_7 chains it could be associated with the onset of oxide ion mobility.

In this paper, we report a study on the structural properties and conductivity of a family of compounds derived from $Ba_3YGa_2O_{7.5}$. We determine the room temperature structures using powder neutron diffraction and show that a structural transition involving rearrangement of the oxide ions occurs at high temperature. We report the first studies on the conductivity of an $A_3OhTd_2O_{7.5}$ compound, which reveal both oxide and proton contributions to the conductivity of $Ba_3YGa_2O_{7.5}$. The effect of substitution on the A, Oh and Td site is investigated and compositions such as $Ba_{2.9}La_{0.1}YGa_2O_{7.55}$ and $Ba_3YGa_{1.9}Ti_{0.1}O_{7.55}$ are found to have significantly enhanced oxide ion conductivity.

EXPERIMENTAL

Synthesis. 2 g polycrystalline samples of $Ba_3YGa_2O_{7.5}$ (BYGO) were synthesized from stoichiometric amounts of $BaCO_3$ (Fisher Scientific, 99%), Y_2O_3 (Sigma Aldrich, 99.99%) and Ga_2O_3 (Sigma Aldrich, ≥ 99.99%). Starting compounds were ground together in ethanol, pelletized and heated in alumina crucibles at 1200 °C for 12–18 h. Samples were reground, re-pelletized and reheated until no changes in the powder X-ray diffraction pattern occurred, requiring a maximum heating time of 180 h. For neutron diffraction, the same method was scaled up to 10 g batches.

The substituted series $Ba_{3-x}La_xYGa_2O_{7.5+0.5x}$ (x = 0.05, 0.1, 0.15, 0.2, 0.5), $Ba_3YGa_{2-x}Ti_xO_{7.5+0.5x}$ (x = 0.05, 0.1, 0.15, 0.2), $Ba_3YGa_{2-x}Zn_xO_{7.5-0.5x}$ (x = 0.1), $Ba_3YGa_{2-x}Ge_xO_{7.5+0.5x}$ (x = 0.1) and $Ba_3Y_{1-x}Zr_xGa_2O_{7.5+0.5x}$ (x = 0.05, 0.1) were made using the same method using La_2O_3 (Acros Organics, 99.99%), TiO_2 (Aldrich, ≥ 99.5%), ZnO (Alfa Aesar, 99.99%), GeO_2 (Acros Organics, 99.999%) and ZrO_2 (Aldrich, 99 %). La_2O_3 was dried at 1000 °C for 12 h prior to weighing. Compounds were heated for a maximum of 300 h but those that formed single phases needed < 100 h total heating time.

X-ray diffraction. A Bruker D8 Advance diffractometer in Bragg-Brentano geometry using Cu Kα radiation and a Lynx-eye PSD detector was used for all ambient-temperature X-ray diffraction. An internal Si standard (a = 5.431195(9) Å at room temperature) was used for accurate cell parameter determination. Analysis of the diffraction data was performed using the Rietveld method[41] implemented in the Topas Academic software.[42-43]

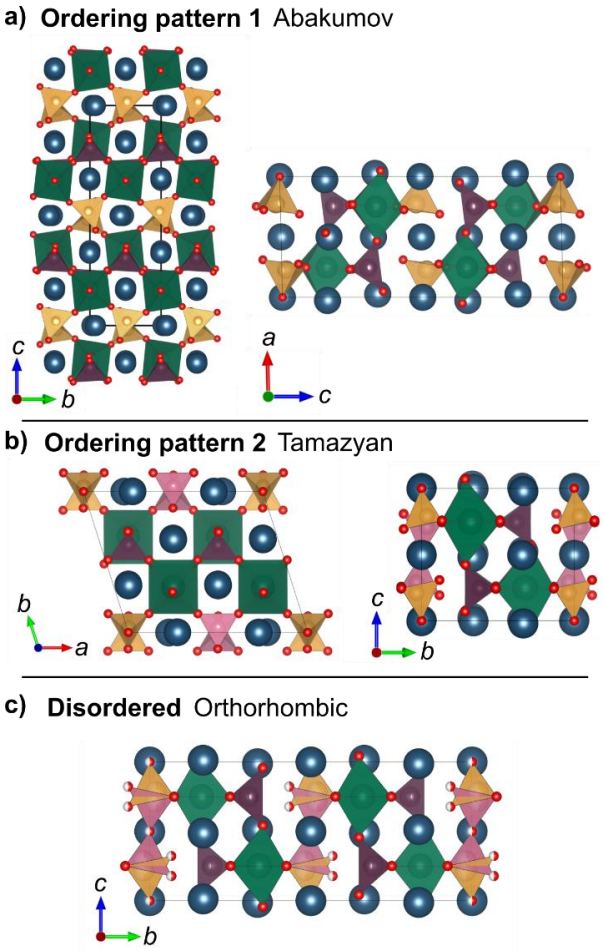

Figure 2. Examples of different ordering patterns in the Td_2O_7 layers. The two possible positions for Td_2O_7 groups are shown in yellow and pink.

Variable-temperature X-ray diffraction patterns were recorded over a temperature range of 25–1000 °C in 20 °C steps with an Anton Paar HTK1200 furnace attachment. Furnace temperatures were calibrated with an external Al_2O_3 standard and held constant during each measurement.[44] Diffraction data were measured for $10 \le 2\vartheta \le 120°$ in 0.02° steps on heating and cooling for between 20 min and 3 h for all single-phase samples. All resulting diffraction patterns were analyzed by sequential Rietveld fitting in Topas Academic. Thermal expansion coefficients were extracted by numerical differentiation of smooth (spline) fits to the experimental cell parameters.

Neutron diffraction and total scattering. 10 g powdered samples of $Ba_3YGa_2O_{7.5}$ and $Ba_{2.9}La_{0.1}YGa_2O_{7.55}$ were synthesized for neutron total scattering experiments. Once phase purity was achieved, the samples were dried at 1200 °C overnight then quench-cooled to room temperature. ~6 g of each sample was then immediately sealed in 8 mm diameter vanadium cans, and data collected on the POLARIS instrument of the ISIS facility at the Rutherford Appleton Laboratory.

High-quality datasets for pair distribution function (PDF) analysis were acquired for each sample at room temperature and 1000 °C for 8 h each. Scattering due to the sample can was measured for 2 h at room temperature and scattering from the empty sample can in the furnace, and the empty furnace were measured at room temperature for 8 h and 5 h, respectively. While heating to 1000 °C, short 15 min datasets were collected on both samples for Rietveld analysis of the Bragg scattering.

Neutron total scattering data were normalized onto an absolute scale using GudrunN software;[45] the $D(r)$ functions used for fitting were extracted by merging data from all detector banks using standard formalisms[46] resulting in a usable Q_{max} of between 35 and 39 Å^{-1}; Fourier ripples at r ≤ 1.1 Å were removed. Bragg data were extracted using the established analysis routines in Mantid.[47]

All structural analyses were performed using Topas Academic. Rietveld fits were performed using the three highest resolution data banks (banks 3, 4, and 5; detector 2ϑ angles 52.2°, 91.5°, 146.9°; d_{max} ≈ 5.1 Å, 3.5 Å, 2.7 Å, respectively) of POLARIS, covering a total d-spacing range of 0.15–5.0 Å. Bank 4 was selected for the combined analysis of Bragg and PDF data as it offers a good compromise between resolution and Q-range. Rietveld models were expanded into large-box models by constructing supercells that were as close to isotropic as possible. Each model contained approximately 2500 atoms. Where the Rietveld model reflected some disorder in the structure, in-house C++ code was used to distribute atoms appropriately based on random number generators. Atomic coordinates were then refined against the data subject to bond length and angle restraints with a χ^2 penalty applied if the local geometry deviated too much from the ideal. The ideal angles were those in perfect octahedra or tetrahedra, and the ideal bond lengths calculated from bond valence sums as appropriate. Bragg (from bank 4) and PDF datasets were fitted simultaneously using a fitting range of 4000–19500 μs (d = 0.75–3.6 Å) for Bragg data and 0–30 Å for PDF $D(r)$ data. In initial refinement cycles, coordinate changes were constrained to prevent large atomic shifts; these constraints were relaxed during fitting. An equal weighting was applied to each point in the PDF such that the PDF and Bragg data gave a similar contribution to the overall χ^2. PDF patterns were calculated directly from the atomic coordinates of the large box model, and the Bragg scattering was calculated by folding the large-box coordinates back into a single crystallographic unit cell.

Scanning Transmission Electron Microscopy (STEM). AC-STEM data in Z-contrast HAADF (high-angle annular dark-field) imaging mode was collected from powdered $Ba_3YGa_2O_{7.5}$ samples. The powder was lightly ground in an agate mortar and pestle before loading onto holey carbon-coated Cu TEM grids. A JEOL JEM2100F with a CEOS aberration corrector for the electron probe was used at 200 kV to image the sample.

Thermogravimetric analysis. Mass changes on heating and cooling from 30 to 1000 °C at 10 °C min^{-1} under flowing dry air were measured using a PerkinElmer TGA 8000 instrument. Experiments were performed on freshly cooled $Ba_3YGa_2O_{7.5}$ (heated at 1150 °C for 8.5 h and cooled to 150 °C at 5 K min^{-1}) and on samples of $Ba_3YGa_2O_{7.5}$, $Ba_3YGa_{1.9}Zn_{0.1}O_{7.45}$ and $Ba_{2.9}La_{0.1}YGa_2O_{7.55}$ after exposure to laboratory air for 3 days.

Solid State ^{1}H NMR. The hydration behavior of $Ba_3YGa_2O_{7.5}$ was investigated using proton NMR. The sample was heated to 1000 °C for 12 h then quench-cooled to room temperature. The ^{1}H NMR spectrum was recorded immediately on a Bruker Avance III HD spectrometer with tetramethylsilane as a reference. The sample was then placed in a 74% relative humidity chamber for 1 week, and the proton spectrum was re-collected under the same conditions.

Impedance spectroscopy. Powders for impedance measurements were uniaxially pressed into 10 mm pellets and sintered. Samples, sintering times and temperatures, and final densities are given in Table S1. Each pellet was coated in platinum ink and mounted on a Probostat A-6 cell. The electrodes were set by heating at 1000 °C for 1 h. A Solartron 1260 frequency-response analyzer was used to measure and record impedance spectra approximately every 20 °C. Frequency ranges of 0.1–10^7 Hz and voltages of 100–1000 mV were used for the measurements, and results were analyzed in ZView (Scribner Associates). For standard measurements, the impedance was recorded on cooling at 2 °C min^{-1} from 1000 °C to room temperature in air. Where necessary, further measurements were then performed on heating back to 1000 °C. The impedance of certain samples was also measured under dry flowing N_2, and/or wet N_2 (pH_2O ≈ 0.021 atm). Where gases were used, the impedance was recorded over multiple heating and cooling cycles to ensure equilibrium had been achieved. The details of experiments performed for each sample are in Table S1.

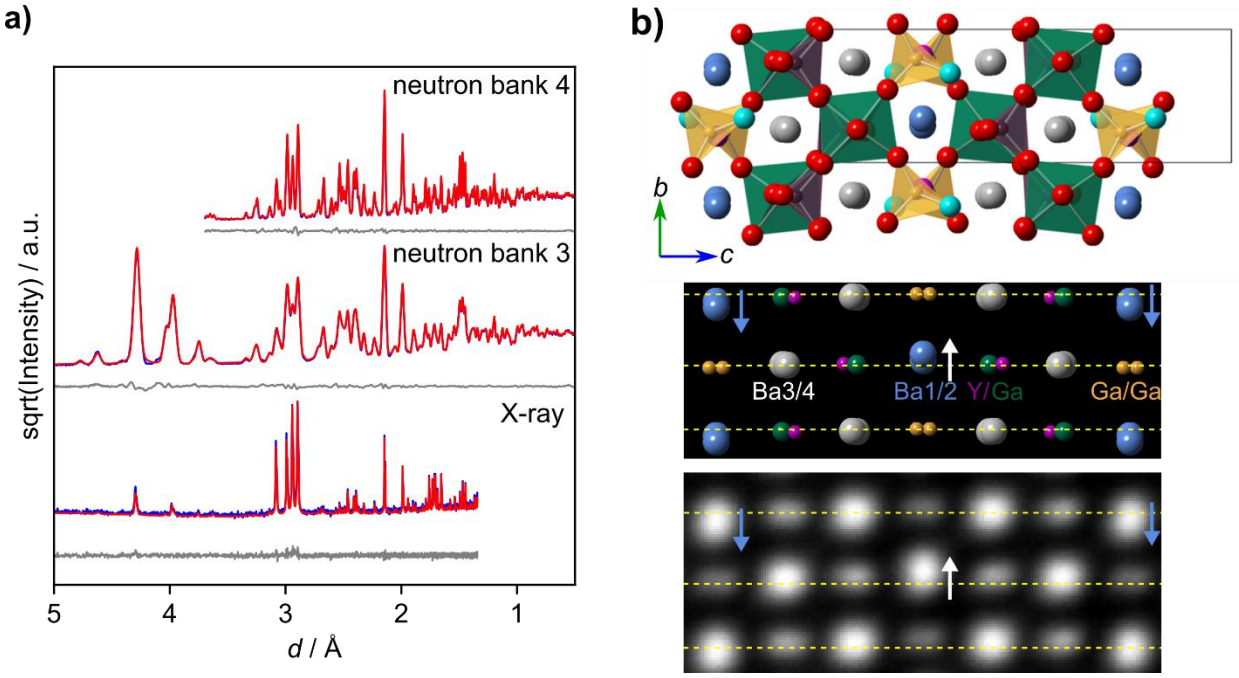

Figure 3. a) Joint Rietveld refinement against multibank neutron and X-ray diffraction patterns of $Ba_3YGa_2O_{7.5}$ collected at room temperature. b) View of the refined structure and corresponding HAADF-STEM image; blue and white arrows are used to emphasize Ba positions relative to the dotted yellow lines. In a) blue, red and grey curves are observed, calculated and difference plots, respectively.

RESULTS AND DISCUSSION

Ambient structure of $Ba_3YGa_2O_{7.5}$. We are only aware of a single structural model of an $A_3LnGa_2O_{7.5}$ compound: that of $Ba_3ErGa_2O_{7.5}$ reported by Abakumov where the *P*2/*c* space group and unit cell were confirmed by electron diffraction and the structure determined by Rietveld refinement against laboratory X-ray diffraction data.[33] Figure 3a and Table S2 show the results of a joint structural refinement against X-ray and neutron data for $Ba_3YGa_2O_{7.5}$ (BYGO) starting from this model. Neutron datasets from the three highest resolution detector banks (3-5) on POLARIS and a laboratory X-ray dataset were simultaneously fitted, with neutron and X-ray data weighted such that they contributed roughly equally to the overall χ^2. Cell parameters, atomic coordinates and individual isotropic atomic displacement parameters were refined, yielding a final R_{wp} of 3.07%. There were no features of the diffraction patterns that were not fitted with this model, and thus it is a satisfactory description of BYGO at room temperature. Bond distances and angles (Table S3) and bond valence sums are within expected ranges. The local structure of BYGO was also investigated using total neutron scattering (PDF analysis). This confirmed (Figure S2) that the average structure model also describes the local structure well at room temperature.

The structural model was also investigated by HAADF STEM imaging. Figure 3b shows an image corresponding to a single unit cell viewed down the *a*-axis averaged from a larger area image containing 106 unit cells (see Figure S1). Similar images were obtained from all crystallites studied. Bright spots correspond to columns of Ba, Y/Ga and Ga atoms in the structure. The "up/down" displacement of Ba columns observed experimentally (shown in Figure 3b with white/blue arrows emphasizing shifts relative to the yellow dashed guide lines) is consistent with the Rietveld model. The "stretched" ellipses observed for Y/Ga and Ga columns are consistent with the Rietveld-derived offsets of these sites along the *c*-axis, while their tilts relative to the yellow dashed lines are consistent with the Rietveld-derived offsets along the *b*-axis.

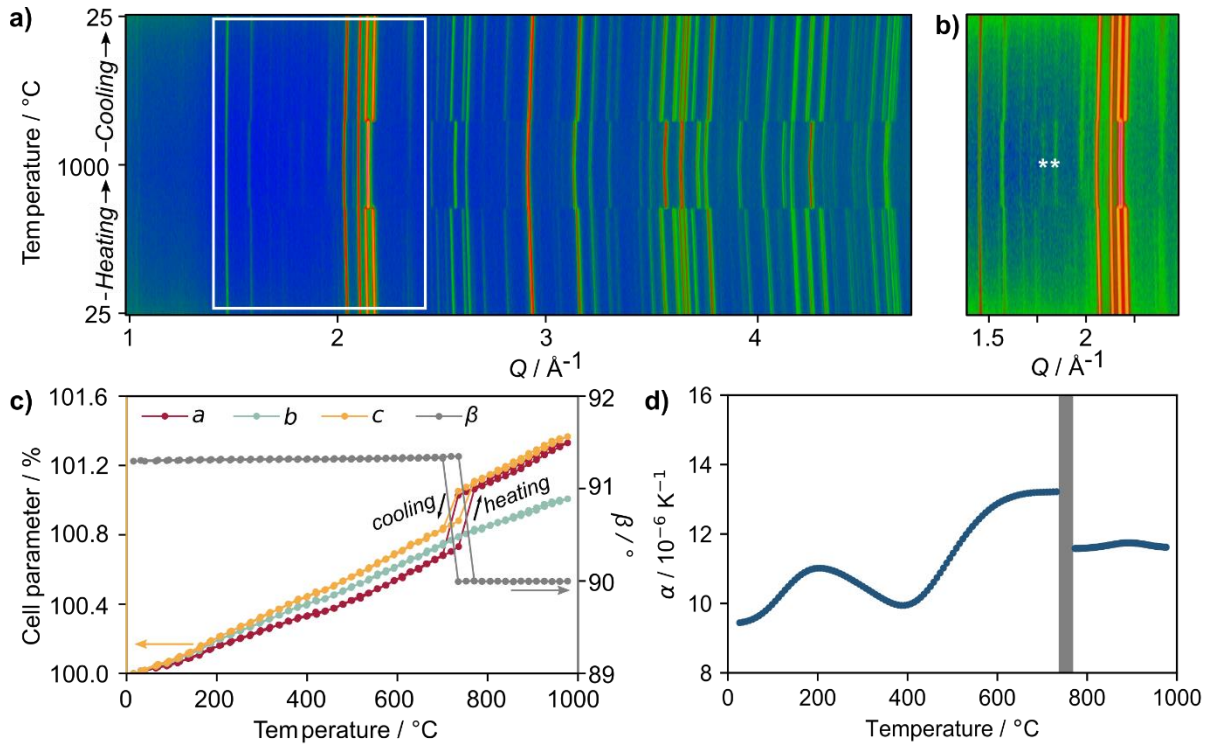

Figure 4. a) Powder X-ray diffraction patterns of $Ba_3YGa_2O_{7.5}$ as a function of temperature as a color map with blue and red colors showing low and high intensity respectively. b) A zoom of the region in the white box plotted on a logarithmic scale to highlight the appearance of the asterisked peaks above the phase transition. c) The derived cell parameter changes. d) The volume thermal expansion coefficient, α_V. No thermal expansion data is shown in the shaded region where the phase transition occurs.

High temperature structure. Variable temperature diffraction was performed to investigate any high-temperature structural changes that might have implications on the ionic conductivity of BYGO. The variable temperature X-ray diffraction pattern and derived unit cell parameters are shown in Figure 4. The data clearly show a first order phase transition between 757 and 770 °C on heating, revealed by merging of various reflections, including the two most intense. Additionally, some weak peaks at Q = 1.75, 1.82, 1.93 and 2.23 Å^{-1} appear above the phase transition; these are highlighted in Figure 4b and can be clearly seen on a logarithm scale. Phase transitions have not been reported previously in Ga-containing compositions.[28,29] For convenience we will label the low and high temperature phases as α and β, respectively.

The cell parameters in Figure 4c were extracted by Rietveld fitting our $P2/c$ model to each dataset. They show an abrupt increase in a and c cell parameters and a decrease in cell angle β to 90.0° at the phase transition; β = 90 suggests a change to orthorhombic symmetry at high temperature. The transition is fully reversible, with room temperature patterns before and after heating matching well. Thermal hysteresis, consistent with the first order nature of the transition, is observed with the phase transition on cooling ~20 °C lower (736–757°C) than on heating. This hysteresis seems substantially larger than that reported for $Ba_3NdAl_2O_{7.5}$, which was no greater than 2 °C,[33] although measurements intervals of 20°C intervals mean that there is a significant margin of error. The volume thermal expansion coefficient is displayed in Figure 4d, using data from both cooling and heating experiments. Features similar to the "hump" at 200 °C have been attributed to water uptake in other materials.[24] The fact that data on heating and cooling overlay perfectly suggest that, if this is caused by water uptake, equilibration with atmospheric moisture occurs on the experimental timescale (approximately 30 minutes per pattern).

The most obvious choice for the high temperature structure would be the disordered orthorhombic $Cmcm$ structure shown in Figure 2c. However, neither this model, nor any subgroups with the same unit-cell size can explain the four weak peaks observed at high temperature. We find, however, that the positions and intensities of these peaks can be fully explained by a model with Tamazyan type ordering of Td_2O_7 groups in space group $P112_1/a$. Figure 5 shows Rietveld fits to neutron and X-ray data collected at 1000 °C, with the weak additional peaks highlighted. The monoclinic angle of this unit cell refines to γ=107.844(3)°, which corresponds to an angle of β=89.986(3)° when transformed to an equivalent setting to the low temperature α $P2/c$ unit cell. We therefore conclude that for this composition the apparent monoclinic to orthorhombic transition is in fact a first order transition from monoclinic $P2/c$ to monoclinic $P112_1/a$ caused by a change in Td_2O_7 ordering.

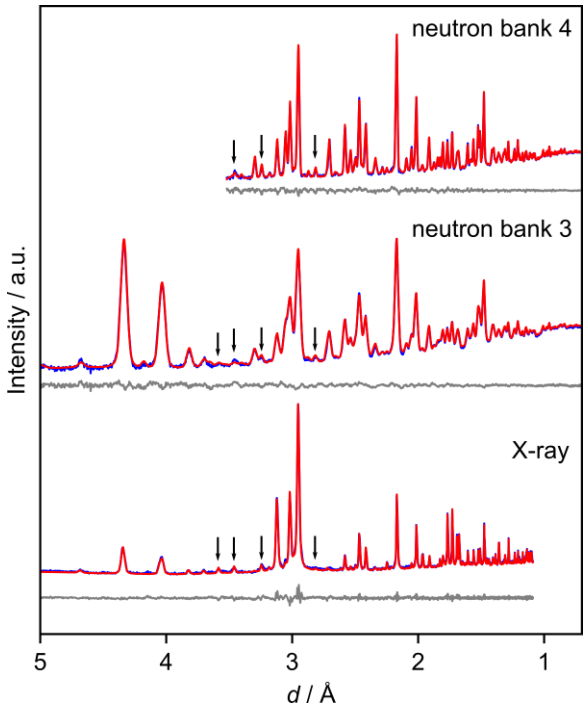

Figure 5. Rietveld fits of X-ray and two neutron datasets. Arrows indicate the peaks fitted by the Tamazyan model but not the *Cmcm* or Abakumov models.

The possibility of oxygen disorder along the Td_2O_7 chains parallel to *a* (Abakumov cell) was investigated by allowing partial occupancies of sites associated with the alternative yellow and pink tetrahedra of Figure 2c during the Rietveld fitting. Free refinement converged to an ~80:20 distribution of Tamazyan and Abakumov ordering, respectively. PDF and Rietveld analysis at 1000 °C (Figure S2) shows the expected increase in thermal motion of O1 (Td-O1-Td) and O8 (terminal) oxygen sites at high temperature, but we see no evidence for the much more significant oxygen disorder that would be associated with a *Cmcm* structure. As shown in Figure 2b, the β-$Ba_3YGa_2O_{7.5}$ structure has a significant "unwinding" of polyhedral tilts relative to the low temperature α structure, with Ga_2O_7 groups close to a staggered configuration and octahedra and tetrahedra of the YO_6/GaO_4 slabs essentially untilted. The structural changes at the phase transition thus provide a potential mechanism for the twinning observed by high resolution electron microscopy in related compositions by Abakumov.[33]

Water uptake in $Ba_3YGa_2O_{7.5}$. Water uptake in anion deficient perovskites is important both in terms of proton conductivity (see below) and sample stability. TGA studies recorded immediately after cooling samples in air from 1150 °C over 3 h showed a gradual 0.3% mass loss up to 950 °C on reheating under dry air (Figure S3). This is consistent with a low level of water retention to high temperature. BYGO is stable when stored in sealed vials at room temperature and under the high temperature conditions used for the diffraction studies of Figure 4 and the conductivity studies discussed below. BYGO will, however, react with atmospheric moisture over longer periods at room temperature. In situ X-ray studies (Figure S4) suggest a stability half-life of around 10 h, such that it can be handled in normal atmospheres for short periods without issues. TGA experiments on a sample deliberately exposed to moisture until it became X-ray amorphous (Figure S5, S6) showed a mass loss of ~19.5% on reheating to 1000 °C. This is consistent with a composition of~$Ba_3YGa_2O_{7.5}{\cdot}10H_2O$, or the water content required to fully convert to metal hydroxides (e.g. $3Ba(OH)_2.H_2O + Y(OH)_3 + 2Ga(OH)_3$ or equivalent mixed metal hydroxides would correspond to $10.5H_2O$). Proton uptake is confirmed by solid state NMR (Figure S7), but we can't rule out additional carbonate formation. In situ powder diffraction experiments during dehydration of this amorphous sample on heating (Figure S8) showed crystallization events coinciding with TGA mass losses and the rapid reformation of BYGO at ~900 °C.

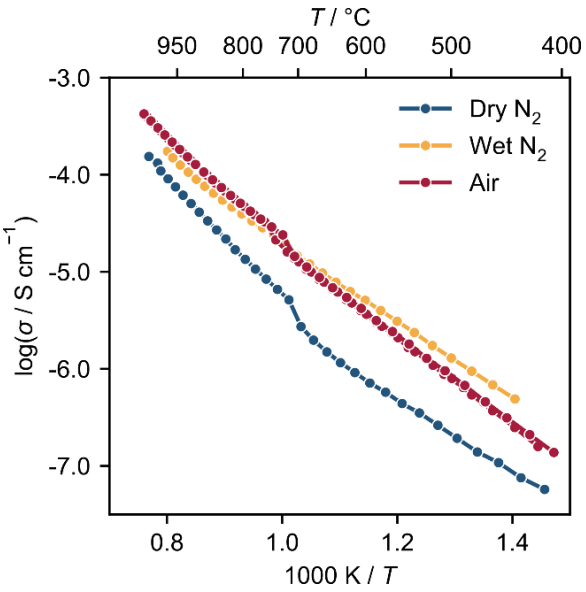

Figure 6. Arrhenius plots of the conductivity of $Ba_3YGa_2O_{7.5}$ in different atmospheres.

Conductivity of $Ba_3YGa_2O_{7.5}$. Initial conductivity measurements were performed on BYGO using impedance spectroscopy under air, and both dry and wet N_2 atmospheres. Results are given in the log plot of Figure 6, and show that BYGO attains a conductivity of $4.5{\times}10^{-5}$ S cm^{-1} at 800 °C. The α→β structural phase transition is revealed in the plot as a small discontinuous change in conductivity at ~750 °C. This suggests that the reordering of the Ga_2O_7 groups influences the conductivity; however, the increase is relatively small. This implies a largely ordered high temperature phase as opposed to significant dynamic disorder, consistent with our structural studies. Data measured in different heating and cooling cycles coincided except close to the phase transition, where small thermal hysteresis was seen. Activation energies extracted from $\log(\sigma T)$ vs $1/T$ above and below the phase transition were 1.09(2) and 0.921(3) eV, respectively.

The conductivity under wet N_2 is comparable to that in air with a similar small discontinuity at the α→β phase transition. Under dry N_2 we see a reduction in conductivity which suggests a significant proton contribution in moist atmospheres. This could occur via a $O_O^X + H_2O + V_O^{\cdot\cdot} \rightarrow 2OH_O^{\cdot}$ type hydration or H_2O uptake into sites between Td_2O_7 groups; either could give rise to mobile protons. The proton contribution reduces at high temperature but does not fall to zero, consistent with the TGA data of Figure S3. This kind of high-temperature proton conductivity is seen in perovskite-type compounds such as $BaZrO_3$, $SrZrO_3$ and $SrCeO_3$ which show a significant proton contribution up to at least 850 °C.[48-49] We note, however, that proton/oxide conductors such as $BaZr_{1-x}Y_xO_{3-\delta}$ have a significant hole contribution to their conductivity at high pO_2.[50-51] We can't fully exclude a similar hole contribution in BYGO purely from these data.

Table 1. Purity of substituted compositions from PXRD; oxygen content is calculated by charge balance.

>99% $A_3OhTd_2O_{7.5}$	>90% $A_3OhTd_2O_{7.5}$	<90% $A_3OhTd_2O_{7.5}$
$Ba_{2.95}La_{0.05}YGa_2O_{7.525}$	$Ba_{2.85}La_{0.15}YGa_2O_{7.575}$	$Ba_{2.5}La_{0.5}YGa_2O_{7.75}$
$Ba_{2.9}La_{0.1}YGa_2O_{7.55}$*	$Ba_{2.8}La_{0.1}YGa_2O_{7.6}$	
$Ba_3YGa_{1.95}Ti_{0.05}O_{7.525}$	$Ba_3YGa_{1.85}Ti_{0.15}O_{7.575}$	
$Ba_3YGa_{1.9}Ti_{0.1}O_{7.55}$*	$Ba_3YGa_{1.8}Ti_{0.2}O_{7.6}$	
$Ba_3YGa_{1.9}Zn_{0.1}O_{7.45}$*	$Ba_3YGa_{1.9}Ge_{0.1}O_{7.55}$	
$Ba_3Y_{0.95}Zr_{0.05}Ga_2O_{7.525}$*	$Ba_3Y_{0.9}Zr_{0.1}Ga_2O_{7.55}$	

Increasing conductivity through chemical substitution. Several compounds substituted with a variety of acceptor (Zn^{2+} on Td) or donor (La^{3+} on A, Zr^{4+} on Oh, Ti^{4+} on Td) species were prepared with the aim of improving conductivity through the introduction of extra oxygen vacancies or interstitial oxygen defects. A summary of the compositions targeted, and sample purities achieved is given in Table 1.

The room-temperature diffraction patterns of all substituted materials could be fitted well with the *P*2/*c* model indicating the substituent elements are in a low enough concentration not to induce major structural changes. Cell parameters of each composition were obtained by X-ray diffraction on dry samples using a Si internal standard. The resulting cell volumes are plotted in Figure S10.

Single phase compositions with the highest substituent content (indicated by a * in Table 1) were chosen for further investigation. Variable temperature diffraction shows that all the compositions with interstitial oxygens have similar temperature-dependent behavior to BYGO, exhibiting a similar abrupt change in cell parameters at the α→β phase transition. The temperature of the phase transition is not greatly affected by the presence of the substituent and occurs at 750±20 °C (i.e. within one temperature step) for all the compounds measured. Above the phase transition, substituted compounds display the weak peaks associated with Tamazyan-type ordering, and the structures of $Ba_{2.9}La_{0.1}YGa_2O_{7.55}$ above and below the phase transition was confirmed using neutron and X-ray diffraction. We attempted to locate the additional O sites from PDF-quality neutron diffraction data by introducing excess oxygen at sites midway between Ga_2O_7 groups. However, the relatively low excess oxygen content, equivalent to 0.2 additional O per unit cell on average, gave insufficient contributions to the scattering to definitively locate these atoms. Figure S11 shows the neutron Bragg and PDF fits using this model.

Figure S12 shows the temperature evolution of selected cell parameters extracted by Rietveld refinement. $Ba_3YGa_{1.9}Zn_{0.1}O_{7.45}$ shows somewhat different behavior to the other compounds. There is a significant deviation from the expected trend in the *a* cell parameter between 200 and 400 ° C followed by a gradual decrease in *β* before the phase transition at 750 °C. This behavior is consistent with the additional vacancies caused by lower-valent Zn substitution and its higher basicity leading to additional water uptake at low temperatures. It is known from other systems that Zn incorporation can increase H_2O uptake, even beyond the level expected based on the extra vacancies generated.[52] The most striking difference in cell parameter evolution between Zn-substituted and other samples is in the *a*-axis, which is parallel to the chains of Ga_2O_7 groups. This suggests that water sites may be located within these chains.

Conductivity of substituted compounds. The conductivity of each single-phase substituted sample was measured in moist air and under dry flowing N_2 and is shown in Figure 7.

In air, we see that Zr substitution does not improve conductivity relative to BYGO, and the conductivity does not increase significantly at the phase transition. Activation energies remain very similar to BYGO across the temperature range. Zn-substituted $Ba_3YGa_{1.9}Zn_{0.1}O_{7.45}$ again shows a similar conductivity to BYGO at high temperature, but at T ≲ 700 °C the conductivity is up to one order of magnitude higher. This is consistent with a higher proton conductivity contribution and is expected given the cell parameter changes on heating described above. The La- and Ti-substituted excess oxygen compositions both show very different behavior to the other compounds. Both have a larger activation energy than BYGO at low temperatures, a substantial increase in conductivity at the phase transition and an approximate one-order-of-magnitude increase over BYGO at the highest temperatures. The conductivity of $Ba_{2.9}La_{0.1}YGa_2O_{7.55}$ is slightly higher than $Ba_3YGa_{1.9}Ti_{0.1}O_{7.55}$ at all temperatures and it has a lower activation energy above the phase transition. The conductivity of $Ba_{2.95}La_{0.05}YGa_2O_{7.525}$ (not shown) shows similar behavior and lies between BYGO and $Ba_{2.9}La_{0.1}YGa_2O_{7.55}$ at high temperature. BYGO, $Ba_{2.95}La_{0.05}YGa_2O_{7.525}$ and $Ba_{2.9}La_{0.1}YGa_2O_{7.55}$ reach conductivities of 4.5×10^{-5}, 6.9×10^{-5} and 7.9×10^{-4} S cm^{-1} at 800 °C as the interstitials increase from 0 to 0.05 per formula unit.

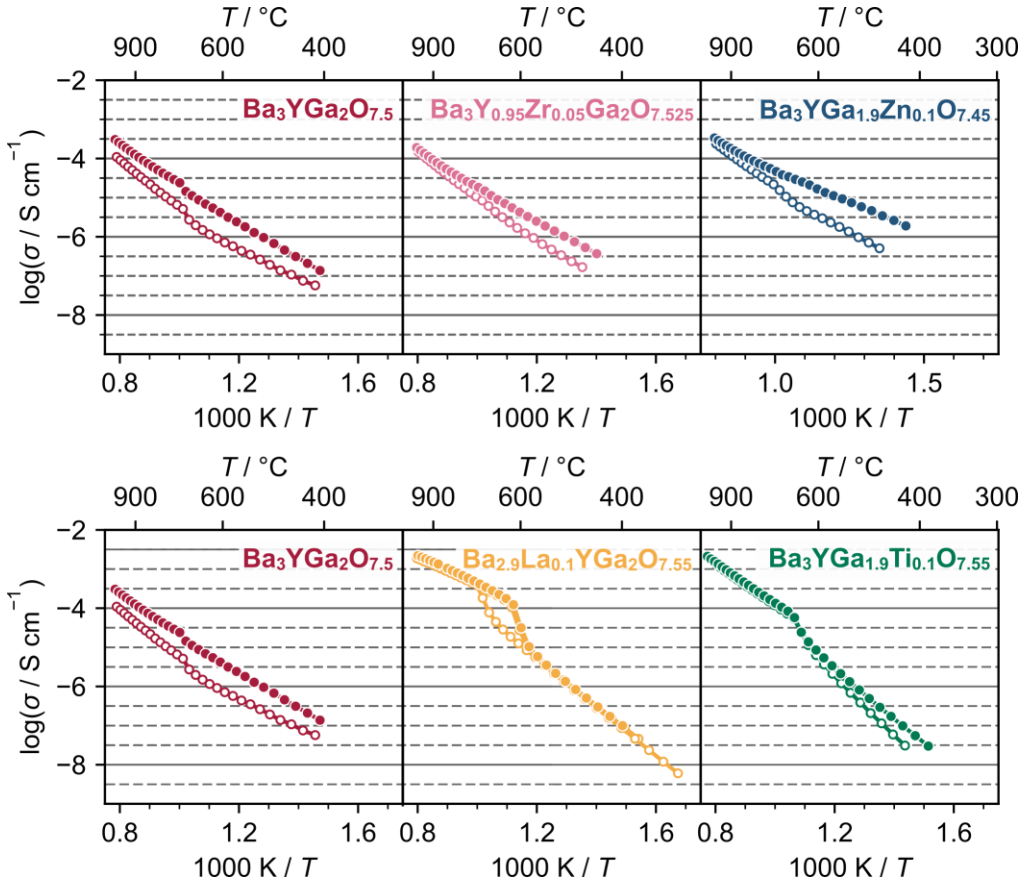

Figure 7. Conductivity of substituted BYGO compounds in air (filled points) and dry N_2 (open points). $Ba_3YGa_2O_{7.5}$ plot is repeated in the lower panel to allow easier visual comparisons with all substituted compounds.

Under dry nitrogen, the high-temperature conductivities of Zr- and Zn-substituted samples are the same as in air, but the low-temperature conductivity is decreased relative to moist atmospheres. This suggests a proton contribution is present up to around 800 °C in both compositions. Above 800 °C, the conductivities are independent of the atmosphere, suggesting oxide ion conductivity dominates. This contrasts with BYGO, where a small proton contribution seems to remain up to 1000 °C. In the absence of this proton contribution, substitution with either Zr or Zn slightly improves the conductivity at all temperatures relative to BYGO. The conductivities of $Ba_{2.9}La_{0.1}YGa_2O_{7.55}$ and $Ba_3YGa_{1.9}Ti_{0.1}O_{7.55}$ are essentially invariant between moist air and dry nitrogen, suggesting they are dominant oxide ion conductors under these conditions.

Pure BYGO is the only compound with a high-temperature conductivity that is different under wet and dry atmospheres at all temperatures. As discussed above, this could be due to a *p*-type electronic conductivity contribution, or a proton conduction contribution retained to an unusually high temperature. *p*-type conduction might be expected to increase for acceptor doping with Zn^{2+}, but this is not observed in $Ba_3YGa_{1.9}Zn_{0.1}O_{7.45}$ whose conductivity appears predominantly due to oxide ions at high temperature. BYGO also shows little difference between the conductivity in moist air and moist N_2. This suggests a proton contribution at high temperature in BYGO, though extensive further studies under controlled pH_2O/pO_2 would be required to confirm this.

CONCLUSIONS

Powdered samples of $Ba_3YGa_2O_{7.5}$ (BYGO) were successfully made using solid state synthesis, and its average room-temperature structure was determined using X-ray and neutron powder diffraction, supported with HAADF-STEM imaging. A phase transition was identified at 750 °C during which the Ga_2O_7 groups in the structure reorder from an Abakumov-type ordering pattern to a Tamazyan-type pattern. The local structure does not deviate significantly from the average structure at room temperature or 1000 °C.

BYGO shows ionic conductivity with $\sigma = 4.5\times10^{-5}$ S cm^{-1} at 800 °C, with a proton contribution amounting to around a half an order of magnitude increase in conductivity in moist atmospheres up to 1000 °C. BYGO needs to be protected from the atmosphere at low temperatures to avoid reaction with moisture, but is stable at the higher temperatures where ionic conductivity is significant. The BYGO structure accepts a range of substituents at <10% level, including those resulting in the incorporation of oxygen vacancies or interstitials. Samples of the substituted compo-

sitions retained the parent structure between room temperature and 1000 °C, exhibiting the same Abakumov-Tamazyan phase transition.

Two types of conductivity behaviors were observed in the substituted samples. Zr- and Zn-substituted compositions retain similar conductivities and activation energies as BYGO, but have slightly altered proton contributions. Zn substitution gives a larger proton contribution below the $\alpha \rightarrow \beta$ phase transition, and this is consistent with water losses inferred from variable temperature diffraction studies. Ti- and La-substituted compositions have a large increase in conductivity around the the $\alpha \rightarrow \beta$ phase transition, making them the most conductive samples at high temperature. The La-substituted sample shows no evidence of proton conductivity, and appears to be an essentially pure oxide ion conductor.

In conclusion, the work reported here shows that materials with the relatively unexplored $A_3OhTd_2O_{7.5}$ structure type show significant proton and oxide-ion conductivity that derives from the unusual structural features associated with their Td-rich composition. The family represents a novel chemically-flexible platform in which to develop new ionic conductors, and the study of related compositions is in progress.

ASSOCIATED CONTENT

Supporting Information. Refined structural parameters for BYGO at room temperature; refined structural parameters for BYGO at 1000 °C; HAADF-STEM images; PDF fits and associated information for BYGO at room temperature and 1000 °C; TGA and diffraction patterns of BYGO when exposed to moisture; ^{1}H NMR spectra of dried and hydrated BYGO; variable temperature XRD patterns of hydrated BYGO; selected complex impedance spectra and experimental details; a comparison of substituted composition cell parameters; PDF fits of $Ba_{2.9}La_{0.1}YGa_2O_{7.55}$ at room temperature and 1000 °C; cell parameters from variable temperature diffraction of substituted compounds. This material is available free of charge via the Internet at http://pubs.acs.org.

AUTHOR INFORMATION

Corresponding Author

* email: john.evans@durham.ac.uk, ivana.radosavljevic@durham.ac.uk.

Present Addresses

†CAF current address: Swiss Norwegian Beamlines at the European Synchrotron Radiation Facility, 71 Av. des Martyrs, 38000 Grenoble, France.

Author Contributions

All authors have given approval to the final version of the manuscript.

Funding Sources

TV and DAB are supported by U.S. ARO Contract # W911NF-20-1-0318.

Notes

No additional relevant notes.

ACKNOWLEDGMENT

We thank Dr. Ron Smith, Dr. Paul Henry and Dr. Helen Playford for help with collecting the neutron diffraction data whilst on-site access was limited due to covid restrictions. We thank Doug Carswell and Dr. David Apperley for assistance with TGA and solid state NMR measurements.

ABBREVIATIONS

BYGO, $Ba_3YGa_2O_{7.5}$.

REFERENCES

1. Yuan, D.; Kröger, F. A., Stabilized Zirconia as an Oxygen Pump. *Journal of The Electrochemical Society* **1969,** *116* (5), 594.
2. Sunarso, J.; Baumann, S.; Serra, J. M.; Meulenberg, W. A.; Liu, S.; Lin, Y. S.; Diniz da Costa, J. C., Mixed ionic–electronic conducting (MIEC) ceramic-based membranes for oxygen separation. *Journal of Membrane Science* **2008,** *320* (1), 13-41.
3. Brett, D. J. L.; Atkinson, A.; Brandon, N. P.; Skinner, S. J., Intermediate temperature solid oxide fuel cells. *Chemical Society Reviews* **2008,** *37* (8), 1568-1578.
4. Woodward, P. M.; Karen, P.; Evans, J. S. O.; Vogt, T., *Solid State Materials Chemistry*. Cambridge University Press: Cambridge, 2021; p 687.
5. Speakman, S.; Richardson, J.; Mitchell, B.; Misture, S., In-situ diffraction study of Ba2In2O5. *Solid State Ionics* **2002,** *149* (3-4), 247-259.
6. Hayashi, H.; Inaba, H.; Matsuyama, M.; Lan, N.; Dokiya, M.; Tagawa, H., Structural consideration on the ionic conductivity of perovskite-type oxides. *Solid State Ionics* **1999,** *122* (1-4), 1-15.
7. Imaizumi, K.; Toyoura, K.; Nakamura, A.; Matsunaga, K., Stable sites and diffusion pathways of interstitial oxide ions in lanthanum germanate. *Solid State Ionics* **2014,** *262*, 512-516.
8. Kendrick, E.; Islam, M. S.; Slater, P. R., Atomic-scale mechanistic features of oxide ion conduction in apatite-type germanates. *Chemical communications (Cambridge, England)* **2008,** *33* (6), 715-717.
9. Peet, J. R.; Chambers, M. S.; Piovano, A.; Johnson, M. R.; Evans, I. R., Dynamics in Bi(III)-containing apatite-type oxide ion conductors: a combined computational and experimental study. *Journal of Materials Chemistry A* **2018,** *6*, 5129-5135.
10. Pramana, S. S.; Klooster, W. T.; White, T. J., Framework interstitial oxygen in $La_{10}(GeO_4)_5(GeO_5)O_2$ apatite electrolyte. *Acta Crystallographica Section B: Structural Science* **2007,** *63* (4), 597-602.
11. Tate, M. L.; Fuller, C. A.; Avdeev, M.; Brand, H. E. A.; McIntyre, G. J.; Evans, I. R., Synthesis and characterisation of new Bi(III)-containing apatite-type oxide ion conductors: The influence of lone pairs. *Dalton Transactions* **2017,** *46*, 12494-12499.
12. Tate, M. L.; Blom, D. A.; Avdeev, M.; Brand, H. E.; McIntyre, G. J.; Vogt, T.; Evans, I. R., New apatite-type oxide ion conductor, $Bi_2La_8[(GeO_4)_6]O_3$: structure, properties, and direct imaging of low-level interstitial oxygen atoms using aberration-corrected scanning transmission electron microscopy. *Advanced Functional Materials* **2017,** *27* (8), 1605625.
13. Auckett, J. E.; Lopez-Odriozola, L.; Clark, S. J.; Evans, I. R., Exploring the nature of the fergusonite-scheelite phase transition and ionic conductivity enhancement by Mo^{6+} doping in $LaNbO_4$. *Journal of Materials Chemistry A* **2021,** *9* (7), 4091-4102.
14. Cheng, J.; Bao, W.; Han, C.; Cao, W., A novel electrolyte for intermediate solid oxide fuel cells. *Journal of Power Sources* **2010,** *195* (7), 1849-1853.
15. Li, C.; Bayliss, R. D.; Skinner, S. J., Crystal structure and potential interstitial oxide ion conductivity of $LnNbO_4$ and

$LnNb_{0.92}W_{0.08}O_{4.04}$ (Ln = La, Pr, Nd). *Solid State Ionics* **2014,** *262*, 530-535.
16. Pramana, S. S.; Baikie, T.; An, T.; Tucker, M. G.; Wu, J.; Schreyer, M. K.; Wei, F.; Bayliss, R. D.; Kloc, C. L.; White, T. J.; Horsfield, A. P.; Skinner, S. J., Correlation of Local Structure and Diffusion Pathways in the Modulated Anisotropic Oxide Ion Conductor CeNbO4.25. *Journal of the American Chemical Society* **2016,** *138* (4), 1273-1279.
17. Toyoura, K.; Sakakibara, Y.; Yokoi, T.; Nakamura, A.; Matsunaga, K., Oxide-ion conduction: Via interstitials in scheelite-type $LaNbO_4$: A first-principles study. *Journal of Materials Chemistry A* **2018,** *6* (25), 12004-12011.
18. Yang, X.; Fernández-Carrión, A. J.; Wang, J.; Porcher, F.; Fayon, F.; Allix, M.; Kuang, X., Cooperative mechanisms of oxygen vacancy stabilization and migration in the isolated tetrahedral anion Scheelite structure. *Nature Communications* **2018,** *9* (1), 1-11.
19. Kuang, X.; Green, M. A.; Niu, H.; Zajdel, P.; Dickinson, C.; Claridge, J. B.; Jantsky, L.; Rosseinsky, M. J., Interstitial oxide ion conductivity in the layered tetrahedral network melilite structure. *Nature Materials* **2008,** *7*, 498-504.
20. Zhou, L.; Xu, J.; Allix, M.; Kuang, X., Development of Melilite-Type Oxide Ion Conductors. *Chemical Record* **2020,** *20* (10), 1117-1128.
21. Kuang, X.; Payne, J. L.; Johnson, M. R.; Evans, I. R., Remarkably high oxide ion conductivity at low temperature in an ordered fluorite-type superstructure. *Angewandte Chemie - International Edition* **2012,** *51* (3), 690-694.
22. Ling, C. D.; Miiller, W.; Johnson, M. R.; Richard, D.; Rols, S.; Madge, J.; Evans, I. R., Local structure, dynamics, and the mechanisms of oxide ionic conduction in $Bi_{26}Mo_{10}O_{69}$. *Chemistry of Materials* **2012,** *24* (23), 4607-4614.
23. Peet, J. R.; Fuller, C. A.; Frick, B.; Koza, M.; Johnson, M. R.; Piovano, A.; Evans, I. R., Insight into Design of Improved Oxide Ion Conductors: Dynamics and Conduction Mechanisms in the $Bi_{0.913}V_{0.087}O_{1.587}$ Solid Electrolyte. *Journal of the American Chemical Society* **2019,** *141* (25), 9989-9997.
24. Evans, I. R.; Howard, J. A. K.; Evans, J. S. O., The crystal structure of α-$La_2Mo_2O_9$ and the structural origin of the oxide ion migration pathway. *Chemistry of Materials* **2005,** *17* (16), 4074-4077.
25. Peet, J. R.; Fuller, C.; Frick, B.; Zbiri, M.; Piovano, A.; Johnson, M. R.; Evans, I. R., Direct Observation of Oxide Ion Dynamics in La2Mo2O9 on the Nanosecond Timescale. *Chemistry of Materials* **2017,** *29*, 3020-3028.
26. Paulus, W.; Schober, H.; Eibl, S.; Johnson, M.; Berthier, T.; Hernandez, O.; Ceretti, M.; Plazanet, M.; Conder, K.; Lamberti, C., Lattice Dynamics To Trigger Low Temperature Oxygen Mobility in Solid Oxide Ion Conductors. *J. Am. Chem. Soc* **2008,** *130*, 16080-16085.
27. Fuller, C. A.; Berrod, Q.; Frick, B.; Johnson, M. R.; Avdeev, M.; Evans, J. S. O.; Evans, I. R., Oxide Ion and Proton Conductivity in Highly Oxygen-Deficient Cubic Perovskite $SrSc_{0.3}Zn_{0.2}Ga_{0.5}O_{2.4}$. *Chemistry of Materials* **2020,** *32* (10), 4347-4357.
28. Hampson, M. R.; Hodgkinson, P.; Evans, J. S. O.; Harris, R. K.; King, I. J.; Allen, S.; Fayon, F., The Nature of Oxygen Exchange in ZrW_2O_8 Revealed by Two-Dimensional Solid-State ^{17}O NMR. *Chemical Communications* **2004,** *0*, 392-393.
29. Araujo, L. R.; Gallington, L. C.; Wilkinson, A. P.; Evans, J. S. O., Phase behaviour, thermal expansion and compressibility of $SnMo_2O_8$. *J. Solid State Chem.* **2018,** *258*, 885-893.
30. Chernov, V. S.; Dobrovolsky, Y. A.; Istomin, S. Y.; Antipov, V. E.; Grins, J.; Svensson, G.; Tarakina, V. N.; Abakumov, A. M.; Van Tendeloo, G.; Eriksson, S. G.; Rahman, S. M. H., Sr_2GaScO_5 $Sr_{10}Ga_6Sc_4O_{25}$, and $SrGa_{0.75}Sc_{0.25}O_{2.5}$: A play in the octahedra to tetrahedra ratio in oxygen-deficient perovskites. *Inorganic Chemistry* **2012,** *51* (2), 1094-1103.
31. Kovba, L.; Lykova, L.; Antipov, E.; Rozova, M., BaO-Ln_2O_3-Al_2O_3 systems. *Zhurnal Neorganicheskoj Khimii* **1984,** *29* (12), 3137-3142.
32. Kovba, L.; Lykova, L.; Rozova, M., BaO-Y_2O_3-Ga_2O_3 system. *Zhurnal Neorganicheskoj Khimii* **1987,** *32* (8), 2011-2013.
33. Abakumov, A. M.; Shpanchenko, R. V.; Lebedev, O. I.; Van Tendeloo, G.; Amelinckx, S.; Antipov, E. V., The phase transitions and crystal structures of $Ba_3RM_2O_{7.5}$ complex oxides (R = rare-earth elements, M = Al, Ga). *Acta Crystallographica Section A* **1999,** *55* (5), 828-839.
34. Luo, K.; Tran, T. T.; Halasyamani, P. S.; Hayward, M. A., Synthesis and Selective Topochemical Fluorination of the Cation and Anion-Vacancy Ordered phases Ba_2YCoO_5 and $Ba_3YCo_2O_{7.5}$. *Inorganic Chemistry* **2013,** *52* (23), 13762-13769.
35. Luo, K.; Hayward, M. A., Complex Cation Order in Anion-Deficient $Ba_nYFe_{n-1}O_{2.5n}$ Perovskite Phases. *Inorganic Chemistry* **2012,** *51* (22), 12281-12287.
36. Ben Yahia, H.; Gaudin, E.; Boulahya, K.; Darriet, J., Synthesis, structure and magnetic properties of the new oxygen-deficient perovskite $Na_3MnV_2O_{7.5}$. *Solid State Sciences* **2011,** *13* (6), 1235-1241.
37. Arroyabe, E.; Kaindl, R.; Többens, D. M.; Kahlenberg, V., $K_2Ca_6Si_4O_{15}$—structural and spectroscopical studies on a mixed tetrahedral–octahedral framework. *Journal of Solid State Chemistry* **2009,** *182* (12), 3254-3261.
38. Wang, C.-H.; Guo, D.-F.; Li, Z.-F.; Wang, X.-M.; Lin, J.-H.; Zeng, Z.-Z.; Jing, X.-P., Crystal structure of $Sr_6Y_2Al_4O_{15}$: XRD refinements and first-principle calculations. *Journal of Solid State Chemistry* **2012,** *192*, 195-200.
39. Tamazyan, R.; Malinovsky, Y.; Sirota, M., Crystal-structure and twinning of $Na_2Ba_6[Si_2O_7][SiO_4]_2$. *Kristallografiya* **1987,** *32* (4), 882-887.
40. Kahlenberg, V.; Maier, M., On the existence of a high-temperature polymorph of $Na_2Ca_6Si_4O_{15}$—implications for the phase equilibria in the system Na_2O-CaO-SiO_2. *Mineralogy and Petrology* **2016,** *110* (6), 905-915.
41. Rietveld, H. M., A profile refinement method for nuclear and magnetic structures. *Journal of Applied Crystallography* **1969,** *2* (2), 65-71.
42. Coelho, A.; Evans, J. S. O.; Evans, I. R.; Kern, A.; Parsons, S., The TOPAS symbolic computation system. *Powder Diffraction* **2011,** *26*, 22-25.
43. Leineweber, A.; Dinnebier, R.; Evans, J. S. O., *Rietveld Refinement, Practical Powder Diffraction Pattern Analysis using TOPAS*. De Gruyter: Berlin/Boston, 2018; p 332.
44. Stinton, G. W.; Evans, J. S. O., Parametric Rietveld refinement. *Journal of Applied Crystallography* **2007,** *40* (1), 87-95.
45. Soper, A. K., GudrunN and GudrunX: programs for correcting raw neutron and X-ray diffraction data to differential scattering cross section. *Rutherford Appleton Laboratory Technical Report* **2011**, RAL-TR-2011-013.
46. Keen, D. A., A comparison of various commonly used correlation functions for describing total scattering. *Journal of Applied Crystallography* **2001,** *34* (2), 172-177.
47. Arnold, O.; Bilheux, J. C.; Borreguero, J. M.; Buts, A.; Campbell, S. I.; Chapon, L.; Doucet, M.; Draper, N.; Ferraz Leal, R.; Gigg, M. A.; Lynch, V. E.; Markvardsen, A.; Mikkelson, D. J.; Mikkelson, R. L.; Miller, R.; Palmen, K.; Parker, P.; Passos, G.; Perring, T. G.; Peterson, P. F.; Ren, S.; Reuter, M. A.; Savici, A. T.; Taylor, J. W.; Taylor, R. J.; Tolchenov, R.; Zhou, W.; Zikovsky, J., Mantid—Data analysis and visualization package for neutron scattering and μ SR experiments. *Nuclear Instruments and Methods in Physics Research Section A: Accelerators, Spectrometers, Detectors and Associated Equipment* **2014,** *764*, 156-166.
48. Ryu, K. H.; Haile, S. M., Chemical stability and proton conductivity of doped $BaCeO_3$-$BaZrO_3$ solid solutions. *Solid State Ionics* **1999,** *125* (1), 355-367.
49. Świerczek, K.; Zając, W.; Klimkowicz, A.; Zheng, K.; Malikova, N.; Dabrowski, B., Crystal structure and proton conductivity in highly oxygen-deficient $Ba_{1-x}La_x(In,Zr,Sn)O_{3-\delta}$ perovskites. *Solid State Ionics* **2015,** *275*, 58-61.

50. Ji, I. H.; Kim, B. K.; Yu, J. H.; Choi, S. M.; Kim, H. R.; Son, J. W.; Lee, H. W.; Lee, J. H., Three dimensional representations of partial ionic and electronic conductivity based on defect structure analysis of $BaZr_{0.85}Y_{0.15}O_{3-\delta}$. *Solid State Ionics* **2011,** *203* (1), 9-17.
51. Nomura, K.; Kageyama, H., Transport properties of $Ba(Zr_{0.8}Y_{0.2})O_{3-\delta}$ perovskite. *Solid State Ionics* **2007,** *178* (7-10), 661-665.
52. Zohourian, R.; Merkle, R.; Raimondi, G.; Maier, J., Mixed-Conducting Perovskites as Cathode Materials for Protonic Ceramic Fuel Cells: Understanding the Trends in Proton Uptake. *Advanced Functional Materials* **2018,** *28* (35), 1-10.